Nonprecious Bimetallic Sites Coordinated on N-Doped Carbons with Efficient and Durable Catalytic Activity for Oxygen Reduction

Shan Yuan, Li-Li Cui, Zhiyu Dou, Xin Ge, Xingquan He, Wei Zhang,* and Tewodros Asefa**

Developing efficient, inexpensive, and durable electrocatalysts for the oxygen reduction reaction (ORR) is important for the large-scale commercialization of fuel cells and metal–air batteries. Herein, a hierarchically porous bimetallic Fe/Co single-atom-coordinated N-doped carbon (Fe/Co-N_x-C) electrocatalyst for ORR is synthesized from Fe/Co-coordinated polyporphyrin using silica template-assisted and silica-protection synthetic strategies. In the synthesis, first silica nanoparticles-embedded, silica-protected Fe/Co-polyporphyrin is prepared. It is then pyrolyzed and treated with acidic solution. The resulting Fe/Co-N_x-C material has a large specific surface area, large electrochemically active surface area, good conductivity, and catalytically active Fe/Co-N_x sites. The material exhibits a very good electrocatalytic activity for the ORR in alkaline media, with a half-wave potential of 0.86 V versus reversible hydrogen electrode, which is better than that of Pt/C (20 wt%). Furthermore, it shows an outstanding operational stability and durability during the reaction. A zinc–air battery (ZAB) assembled using Fe/Co-N_x-C as an air-cathode electrocatalyst gives a high peak power density (152.0 mW cm^{-2}) and shows a good recovery property. Furthermore, the performance of the battery is better than a corresponding ZAB containing Pt/C as an electrocatalyst. The work also demonstrates a synthetic route to a highly active, stable, and scalable single-atom electrocatalyst for ORR in ZABs.

1. Introduction

The cathodic oxygen reduction reaction (ORR) plays a crucial role in many types of renewable energy conversion and storage devices, such as fuel cells and metal–air batteries.[1,2] Unfortunately, the reaction is slow even over Pt, its best precious metal catalyst,[3] and is directly responsible for the limited performances of many of these renewable energy devices. To overcome this issue, and to achieve desirable electrocatalytic performances in these energy systems, relatively high loadings of catalysts (e.g., 0.4 mg of Pt cm^{-2}) are often used. This too has an issue though because Pt is a scarce and an expensive element, and is thus not suitable for large-scale use. It is, therefore, essential to find ways to reduce its loading on electrodes while maintaining its overall activity, and even better, to develop alternative catalysts composed of more abundantly available, inexpensive nonprecious metals.

In recent years, nonprecious metal-based catalysts containing M-N_x-C species (where M represents transition metals coordinated to the N atoms of N-doped carbons) have attracted intense interest due to their outstanding catalytic activity for ORR and excellent stability during the reaction.[4–10] The electrocatalytic activity of such materials for ORR often correlates with the intrinsic activity of the M-N_x-C species or single atoms in them.[11–16] Such single-atom catalysts (SACs) are beneficial because they allow for the catalytic active M-N_x sites to be monodispersed on the carbon support materials, maximizing atom utilization.[1] In particular, single atoms of metals such Fe, Co, or Cu anchored on conductive carbon nanomaterials have recently been reported to show good catalytic activities for ORR.[11,17–24] For example, Han et al. synthesized Fe-N_x-C by pyrolyzing ZIF-8 type metal–organic framework (MOF) composed of Fe-1,10-phenanthroline (Fe-Phen) at 900 °C under an inert atmosphere, and the material showed electrocatalytic activity toward the ORR with an onset potential of 1.05 V versus reversible hydrogen electrode (RHE) and a half-wave potential of 0.91 V vs RHE.[19] The authors also showed that the material could serve as an air cathode catalyst with a high

S. Yuan, Dr. L.-L. Cui, Dr. Z. Dou, Prof. X. He
School of Chemistry and Environmental Engineering
Changchun University of Science and Technology
7089 Weixing Road, Changchun 130022, P. R. China
E-mail: hexingquan@hotmail.com

Dr. X. Ge, Prof. W. Zhang
School of Materials Science and Engineering and
Electron Microscopy Center
Jilin University
2699 Qianjin Street, Changchun 130012, P. R. China
E-mail: weizhang@jlu.edu.cn

Prof. T. Asefa
Department of Chemistry and Chemical Biology &
Department of Chemical and Biochemical Engineering
Rutgers
The State University of New Jersey
610 Taylor Road, Piscataway, NJ 08854, USA
E-mail: tasefa@chem.rutgers.edu

The ORCID identification number(s) for the author(s) of this article can be found under https://doi.org/10.1002/smll.202000742.

DOI: 10.1002/smll.202000742

open-circuit voltage, high power density, and good stability. In another example, Yin et al. synthesized a single-atom Co catalyst on N-doped porous carbon, named Co SAs/N-C(800), by pyrolyzing bimetallic Zn/Co MOF at 800 °C.[21] The material electrocatalyzed ORR even better than Pt/C in terms of half-wave potential. In another example, Du and co-workers synthesized Cu-based SAC dispersed on graphene (Cu/G) with a high loading of Cu (5.4 wt%) that shows a good electrocatalytic activity and durability for the ORR.[22] The authors further indicated that the material displayed a good catalytic activity because it has a large density of highly dispersed single Cu atoms in form of Cu(I)-N_2 sites.

Recent studies have revealed that supporting dual metals on N-doped carbons can result in even more improved electrocatalytic activity for the ORR.[25–31] Compared with the single metallic sites, bimetallic single atoms coordinated with the N-dopant atoms in the carbon materials create more favorable sites for cleaving the bond in O_2 during ORR. For example, Wang et al. developed a host–guest synthetic strategy to construct Fe-Co species supported onto a porous N-doped carbon and the material exhibits a good electrocatalytic activity for the ORR, with a more positive onset potential (1.06 V) and half-wave potential (0.863 V vs RHE) than Pt/C (1.03 V vs RHE and 0.858 V vs RHE).[27] In another example, Zhao and co-workers applied a competitive complexation synthetic strategy to construct a material containing isolated Zn-Co atoms supported on N-doped carbon (Zn/CoN-C). The material showed a good electrocatalytic activity for ORR in both alkaline and acidic media, with half-wave potentials of 0.861 and 0.796 V versus RHE, respectively. Furthermore, the ZAB they prepared using Zn/CoN-C as air cathode gave a peak power density of 230 mW cm^{-2} while exhibiting an excellent durability during its use.[28]

In this contribution, N-doped carbon-supported, atomically dispersed bimetallic Fe/Co sites (Fe/Co-N_x-C) that can efficiently electrocatalyze the ORR are synthesized via pyrolysis of metal-coordinated polyporphyrin with the help of silica nanoparticles templates and silica protection. To achieve an optimized electrocatalytic performance in the material, three synthetic approaches are applied. 1) An all-covalently-assembled porphyrin framework functionalized with bimetallic (Fe,Co) species is used as a precursor to construct N-doped carbon-coordinated monodisperse Fe/Co sites to efficiently utilize the bi-metallic atoms in catalysis. 2) Silica nanoparticles are successfully used as hard templates to produce mesopores, and thereby expose a large density of catalytic active sites and allow for good mass transport for reaction-relevant species, in the material. 3) The silica-protection helps the metal-modified porphyrin framework to maintain its well-defined structure during pyrolysis and form nanostructures with a high density of accessible catalytically active sites. As a result of these, the resulting optimized Fe/Co-N_x-C material possesses a large specific surface area, a large electrochemically active surface area, homogeneously dispersed Fe/Co-N_x bimetallic single-atom sites, and a good electron conductivity. The material also exhibits a very good electrocatalytic activity for ORR in alkaline media and durability during the reaction. Moreover, a home-made ZAB assembled using Fe/Co-N_x-C as an air cathode shows excellent power density while remaining stable for hours.

2. Experimental Section

2.1. Chemicals and Materials

Pt/C (20 wt%) was received from Alfa Aesar. Nafion ionomer solution (5 wt% in ethanol) was obtained from Sigma-Aldrich. 2,5-Dihydroxyterephthaldeyde, pyrrole, hydrophobic SiO_2 nanoparticles (≈30 nm in diameter), $CoCl_2\cdot 6H_2O$, and $FeCl_2\cdot 4H_2O$ were purchased from Aladdin. Hydrochloric acid (37 wt%), dimethyl sulfoxide, *N*,*N*-dimethylformamide, propionic acid, formic acid, tetraethyl orthosilicate (TEOS), and dichloromethane were bought from Beijing Chemical Works. All aqueous solutions were prepared with deionized (DI) water.

2.2. Synthesis of SiO_2@(Fe,Co)PP@SiO_2 and the Corresponding Control Materials

First, SiO_2 nanoparticles (150 mg) were dispersed in propionic acid (10 mL), and the solution was stirred for 10 h before adding 2,5-dihydroxyterephthaldeyde (150 mg) into it. Separately, a solution of dimethyl sulfoxide (1 mL) and propionic acid (20 mL) was prepared. The two solutions were mixed together and stirred until a uniform solution was obtained. Into the solution, 90 µL of pyrrole was slowly added drop by drop under stirring at room temperature. The solution was further stirred for 30 min. It was then heated to 130 °C and kept at this temperature for 2 h to let the polymerization reaction between 2,5-dihydroxyterephthaldeyde and pyrrole occur. The solution was let to cool down to room temperature naturally. The solid product was separated from the solution by suction filtration, and then successively washed with dichloromethane, methanol, and water until the filtrate turned colorless. The crude product was dispersed in ethanol (300 mL) and aged at 2 °C for 12 h. After suction filtration, the obtained solid product was dried under vacuum at 30 °C for 18 h to obtain SiO_2 nanoparticles/polyporyphyrin composite material (SiO_2@PP). Then, SiO_2@PP (30 mg) was mixed with $CoCl_2\cdot 6H_2O$ (157.56 mg, 0.662 mmol) and $FeCl_2\cdot 4H_2O$ (56.40 mg, 0.284 mmol) and *N*,*N*-dimethylformamide (30 mL) with ultrasonication for 30 min. The resulting uniform dispersion was then transferred into a 50 mL Teflon-lined stainless-steel autoclave and kept in oven at 180 °C for 6 h. After letting it cool down to room temperature naturally, the mixture was centrifuged. The solid product was collected and washed successively with distilled water and methanol, and then dried in vacuum at 30 °C for 18 h. Finally, 100 mg of the product was taken and evenly mixed with TEOS (1 mL) with an agate mortar and a pestle. After adding formic acid (1 mL), the mixture was ground till it turned into a powdered material. The material was dried at room temperature giving SiO_2-coated, Fe,Co-coordinated PP@SiO_2, which is denoted as SiO_2@(Fe,Co)PP@SiO_2.

In addition, five other materials, named SiO_2@PP@SiO_2, SiO_2@FePP@SiO_2, SiO_2@CoPP@SiO_2, SiO_2@(Fe,Co)PP, and (Fe,Co)PP@SiO_2, were synthesized using the same procedure except without including $CoCl_2$ + $FeCl_2$, $CoCl_2$, $FeCl_2$, formic acid + TEOS, or SiO_2 nanoparticles, respectively.

2.3. Synthesis of Fe/Co-N$_x$-C and the Corresponding Control Materials

SiO_2@(Fe,Co)PP@SiO_2 was pyrolyzed in a tube furnace under H_2/Ar atmosphere with a volume ratio of 1:9. The pyrolysis was done at 900 °C after raising the temperature from room temperature to 900 °C at a rate of 5 °C min^{-1}, then maintaining it at 900 °C for 2 h. The furnace was then cooled down to room temperature. The product was taken out and treated with HF solution (25%, 30 mL) for 24 h, and subsequently washed with deionized water until the supernatant became neutral. The pyrolyzed materials before and after treatment with HF solution were named SiO_2@(Fe,Co)PP@SiO_2-900-*b* and Fe/Co-N$_x$-C (or SiO_2@(Fe,Co)PP@SiO_2-900), respectively. Two more materials, named SiO_2@(Fe,Co)PP@SiO_2-800 and SiO_2@(Fe,Co)PP@SiO_2-1000, were obtained with the same procedure but by pyrolyzing SiO_2@(Fe,Co)PP@SiO_2 at 800 and 1000 °C, respectively. Five control materials, named SiO_2@PP@SiO_2-900, SiO_2@FePP@SiO_2-900, SiO_2@CoPP@SiO_2-900, SiO_2@(Fe,Co)PP-900, and (Fe,Co)PP@SiO_2-900, were obtained from their respective precursors described in Section 2.2 with the same pyrolysis and etching steps as the ones used to produce Fe/Co-N$_x$-C (or SiO_2@(Fe,Co)PP@SiO_2-900) earlier.

2.4. Electrocatalysis and Electrochemical Measurements

The electrochemical and electrocatalytic tests related to ORR were carried out at room temperature with a CHI 760E electrochemical workstation using a standard three-electrode cell. In the cell, a saturated calomel electrode and a Pt sheet were used as reference and counter electrodes, respectively. Glassy carbon (GC) disks, each with 5 mm in diameter, containing catalyst inks were used as working electrodes. The catalyst inks were prepared as follows. Typically, 1 mg of catalyst was ultrasonically dispersed in absolute ethanol (1 mL) for 2 h to form a homogeneous dispersion of the catalyst. The well-dispersed catalyst ink was pipetted and drop-casted onto a freshly polished GC disk electrode with a catalyst loading of 0.28 mg cm^{-2}. The catalyst-modified electrode surface was then coated with 0.5 wt% Nafion solution (1 µL). Similarly, a working electrode containing a commercially available Pt/C catalyst was prepared for comparative studies. A rotating disk electrode (RDE) and a rotating ring disk electrode (RRDE) spinning at different rates were also used to characterize the electrocatalytic activity of the materials for the reaction.

For the ORR tests, a solution of KOH (0.1 м) that was purged with pure O_2 for at least 30 min was used as an electrolyte. The CV measurements were done in this solution at a scan rate of 50 mV s^{-1}. The electrochemical tests using a RDE were also done in the O_2-saturated KOH solution (0.1 м) by spinning the RDE at different rates, ranging from 200 to 2500 rpm, and by scanning the potential at a rate of 10 mV s^{-1}. The amount of peroxide produced by the reaction and the electron transfer number (n) involved in the reaction were determined by using a RRDE and a potentiostat (Pine Research Instrumentation, Inc.). Electrochemical impedance spectroscopy (EIS) was carried out using the catalyst-modified GC electrode (3 mm in diameter) as the working electrode in an aqueous solution containing 5×10^{-3} м $K_3Fe(CN)_6$ and 0.1 м KCl. The frequency range used for the measurement was 0.01 to 100 kHz and an amplitude of 5 mV. The operational stability of the catalysts was tested by obtaining current versus time (*i–t*) chronoamperometric responses. Accelerated durability test (ADT) of the catalysts was conducted by recording linear sweep voltammetry (LSV) curves of ORR of the material at the 1st and 1500th cycles of CV measurements in O_2-saturated KOH solution (0.1 м) with an electrode rotating at 1600 rpm. During each measurement, iR compensation was automatically applied by the instrument. All the measured potentials were calibrated with respect to the RHE using the equation: E (RHE) = E (Hg/Hg_2Cl_2) + 0.999 V.

2.5. Tests of Electrocatalysts as Air-Cathode Electrodes in ZABs

The ability of the electrocatalysts to serve as air electrode in ZAB was evaluated under ambient condition. To make a home-made ZAB, a Zn foil was polished and used as an anode electrode. As an electrolyte, 6.0 м KOH solution containing 0.2 м $Zn(Ac)_2$ was used. The air-cathode electrode for the ZAB was prepared by loading Fe/Co-N$_x$-C on a carbon paper (1 × 1 cm) which was then coupled with a hydrophobic gas diffusion layer (GDL). The as-prepared catalyst (1 mg) was ultrasonically dispersed in absolute ethanol (1 mL) containing Nafion solution (20 µL) for 6 h. The catalyst ink was then drop-casted on the carbon paper (1 × 1 cm) with a catalyst loading of 1 mg cm^{-2}. For comparison, an air cathode was prepared using a commercially obtained 20 wt% Pt/C catalyst with the same loading (1 mg cm^{-2}), and it was used in an aqueous ZAB in the same way. The performances of both assembled ZABs were tested at room temperature using ambient air at the air-electrode and with a scan rate of 10 mV s^{-1}. While obtaining their LSV curves, iR compensation was automatically applied by the instrument during the measurements. The rate performances of both ZABs were assessed by discharging them at various current densities in the range from 2 to 50 mA cm^{-2}. The long-time galvanostatic discharge performance of the ZAB containing Fe/Co-N$_x$-C as the cathode catalyst was carried out at discharge current densities of 2, 10, and 20 mA cm^{-2}.

2.6. Characterization of Materials

The structure and morphology of the as-prepared materials were characterized using a scanning electron microscope (SEM) (JSM-6701F, JEOL) that is operated at 5 kV and a transmission electron microscope (TEM) (JEM-2010, JEOL) that is operated at 200 kV. High-angle annular dark field-scanning transmission electron microscopy (HAADF-STEM) images were obtained with a JEM-ARM300F Grand ARM Atomic Resolution Electron Microscope (JEOL), equipped with an energy-dispersive X-ray spectrometer (EDS). The crystal structures of the materials were determined with a powder X-ray diffractometer (XRD) (model D/MAX2550VB/PC, Rigaku) that is operated at 40 kV and 15 mA and with Co Kα radiation. The elemental compositions and surface bonding states of the materials were analyzed with an ESCALAB 250 X-ray photoelectron spectrometer (XPS, Thermo Scientific) equipped with a monochromatic Al Kα X-ray source. The degree of graphitization of the materials was obtained with a Lab RAM HR Evolution Raman spectrometer (HORIBA Jobin Yvon) using a 532 nm excitation wavelength. N_2 adsorption–desorption isotherms of the materials were acquired at 77 K using an ASAP 2020 surface area and pore analyzer (Micromeritics).

3. Results and Discussion

The synthetic procedure used to produce Fe/Co-N_x-C catalyst is illustrated in **Scheme 1**. The synthesis starts with the polymerization of 2,5-dihydroxyterephthalic acid and pyrrole in propionic acid in the presence of silica nanoparticles templates. This leads to polyporphyrin (PP)/silica nanoparticles composite material, which is named SiO_2@PP. Then, Fe^{2+}/Co^{2+} ions are coordinated onto the polyporyphyrin in the SiO_2@PP under solvothermal condition to produce SiO_2@(Fe,Co)PP. The SiO_2@(Fe,Co)PP is then evenly mixed with TEOS and formic acid to coat the SiO_2@(Fe,Co)PP with silica via the hydrolysis and condensation of TEOS. The resulting SiO_2-protected material, named SiO_2@(Fe,Co)PP@SiO_2, is pyrolyzed at 900 °C under H_2/Ar atmosphere and then etched with HF solution. This leads to isolated bimetallic (Fe and Co) single atoms coordinated with the N-dopant atoms in the carbon material. This material is Fe/Co-N_x-C or SiO_2@(Fe,Co)PP@SiO_2-900. Two more materials, SiO_2@(Fe,Co)PP@SiO_2-800 and SiO_2@(Fe,Co)PP@SiO_2-1000, are obtained by pyrolyzing the same precursor at 800 and 1000 °C, respectively. Using a similar procedure without including some of the reagents (as detailed in the Experimental Section earlier), five other control materials, named SiO_2@PP@SiO_2-900, SiO_2@FePP@SiO_2-900, SiO_2@CoPP@SiO_2-900, SiO_2@(Fe,Co)PP-900, and (Fe,Co)PP@SiO_2-900, are also synthesized.

Powder XRD patterns of SiO_2@(Fe,Co)PP@SiO_2-900 (or Fe/Co-N_x-C), SiO_2@PP@SiO_2-900, SiO_2@FePP@SiO_2-900, SiO_2@CoPP@SiO_2-900 SiO_2@(Fe,Co)PP@SiO_2-800, and SiO_2@(Fe,Co)PP@SiO_2-1000 all show two broad peaks at 24° and 43° (**Figure 1**a and Figure S1, Supporting Information). These two broad diffraction peaks are associated with the (002) and (101) planes of graphitic carbon. The SEM images reveal that SiO_2@(Fe,Co)PP@SiO_2-900-*b* (before etching with acidic solution) and (Fe,Co)PP@SiO_2-900 (which is synthesized without using silica nanoparticles as templates but with silica protection) show particles with smooth surfaces (Figure S2a,b, Supporting Information). However, the SEM image of SiO_2@(Fe,Co)PP@SiO_2-900 after etching with HF solution (i.e., the material named Fe/Co-N_x-C) shows nanonet morphology with pronounced mesoporous structure (Figure 1b). The mesopores are expected to be beneficial for the mass transfer and exposure of catalytic active sites in it during catalysis. The TEM image of Fe/Co-N_x-C (Figure 1c) further shows a thin nanonet structure that has uniformly sized mesopores with a diameter of ≈30 nm throughout. This observation also points to the silica nanoparticles serving as templates and imprinting the mesopores in Fe/Co-N_x-C. High-resolution TEM (HRTEM) image (inset in Figure 1c) indicates that Fe/Co-N_x-C has an amorphous structure.

The selected area electron diffraction (SAED) pattern of Fe/Co-N_x-C (Figure 1d) shows only rings, indicating the poor crystallinity of the carbon framework in the material. It also shows the absence of crystalline metallic species in the material even if it is pyrolyzed at 900 °C. Further characterization of the pore walls of carbon nanonets using aberration-corrected HAADF-STEM reveals a large number of isolated bright spots with diameters of ≈0.1–0.2 nm (marked with red circles in Figure 1e), indicating the presence of isolated single atoms of Fe and Co within the carbon matrix. Such kinds of single atoms on carbon materials often constitute catalytically active metal-N_x centers.[32] The HAADF-STEM image and the EDS-based elemental mapping (Figure 1f) of Fe/Co-N_x-C show homogeneously distributed Fe, Co, C, N, and O elements within the material.

Raman spectra of Fe/Co-N_x-C and the control materials all show peaks at 1344 and 1589 cm^{-1} (**Figure 2**a and Figure S3, Supporting Information). These peaks correspond to the A_{1g} vibration mode of the disordered carbon (D-band) and the E_{2g} vibration mode of the ordered graphitic carbon (G-band),

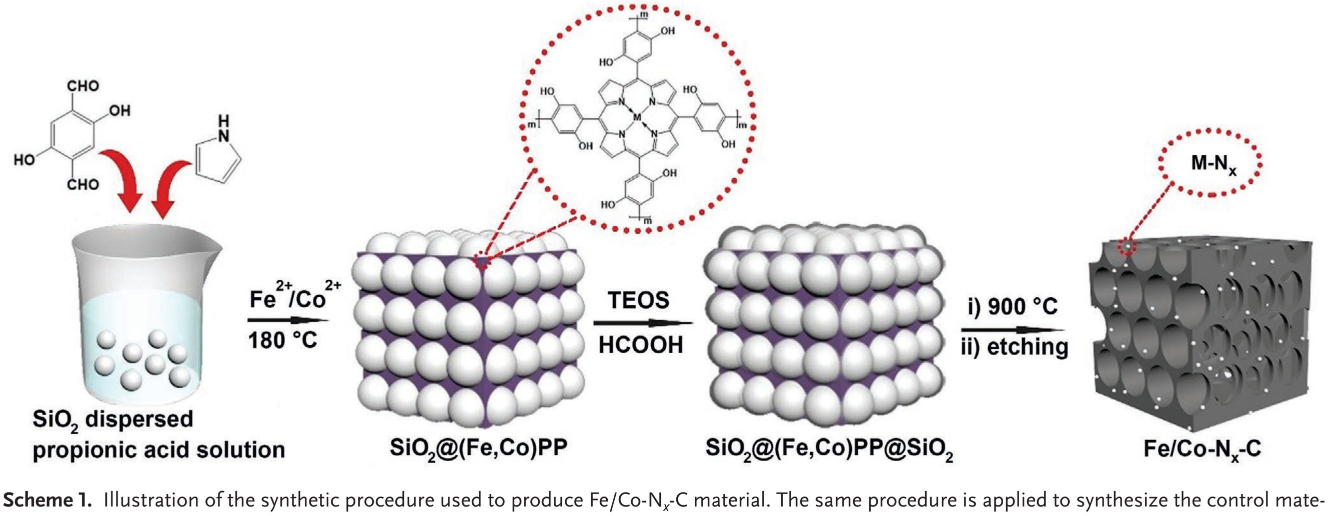

Scheme 1. Illustration of the synthetic procedure used to produce Fe/Co-N_x-C material. The same procedure is applied to synthesize the control materials with a slight change in the compositions of the precursors and pyrolysis temperatures.

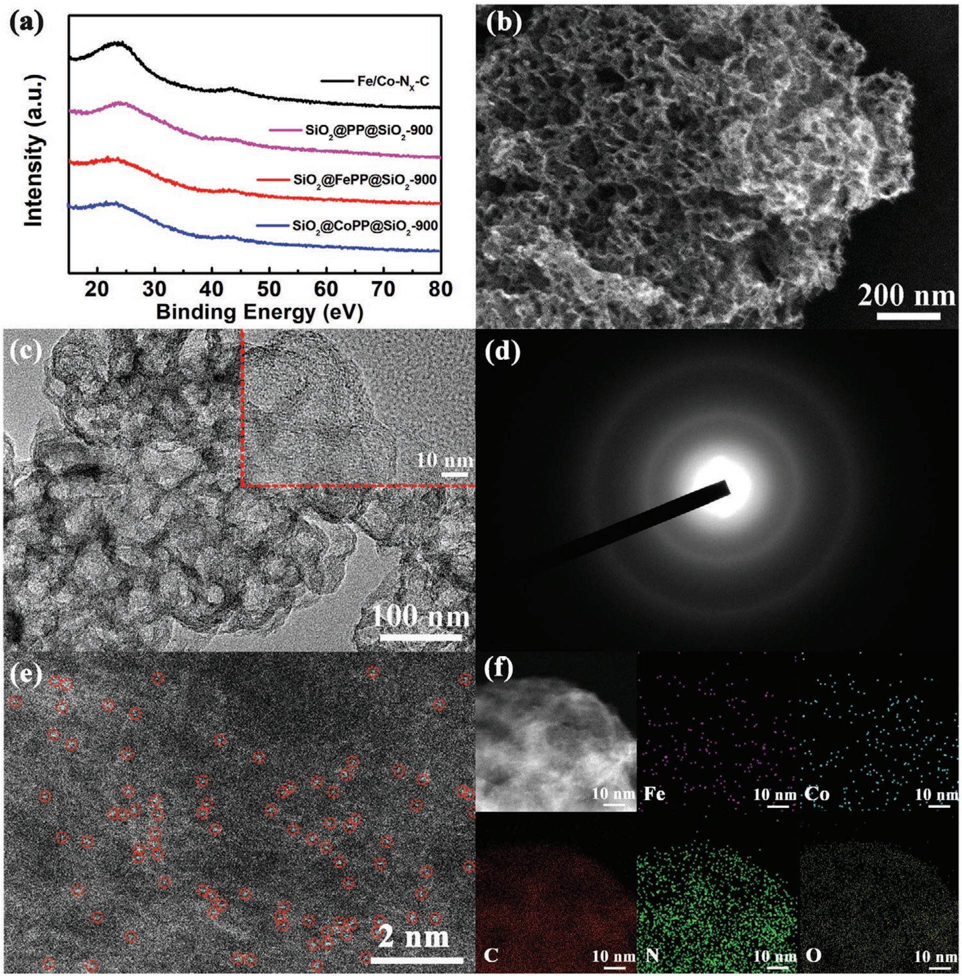

Figure 1. a) XRD patterns of Fe/Co-N$_x$-C (or SiO$_2$@(Fe,Co)PP@SiO$_2$-900), SiO$_2$@PP@SiO$_2$-900, SiO$_2$@FePP@SiO$_2$-900, and SiO$_2$@CoPP@SiO$_2$-900. b) SEM image, c) TEM image, d) SAED pattern, and e) aberration-corrected HAADF-STEM image of Fe/Co-N$_x$-C. f) HAADF-STEM image of Fe/Co-N$_x$-C and EDS elemental mapping images of Fe, Co C, N, and O in it.

respectively.[33] The ratio of the intensities of these two peaks (I_D/I_G) in the spectrum of Fe/Co-N$_x$-C is 1.00, and this value is larger than those of SiO$_2$@PP@SiO$_2$-900 (0.93), SiO$_2$@FePP@SiO$_2$-900 (0.97), and SiO$_2$@CoPP@SiO$_2$-900 (0.98). The results indicate that the introduction of dual-metal atoms in the carbon framework gives rise to slightly more defect sites in the carbon matrix. Such defect sites can be beneficial for the electrocatalytic activity of the materials for ORR.[34]

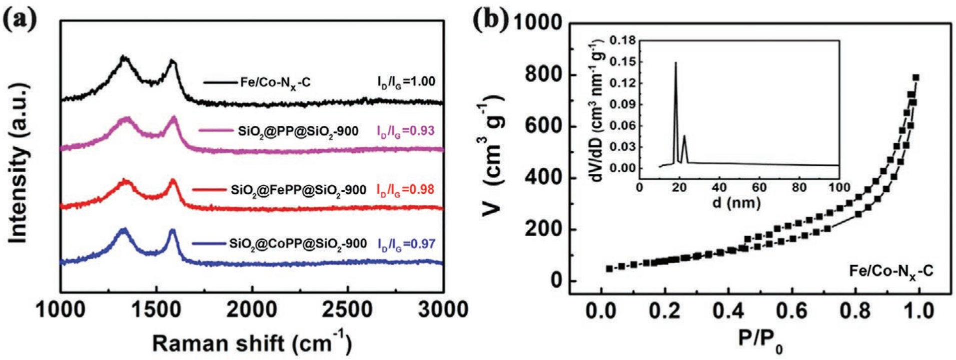

Figure 2. a) Raman spectra of Fe/Co-N$_x$-C, SiO$_2$@PP@SiO$_2$-900, SiO$_2$@FePP@SiO$_2$-900, and SiO$_2$@CoPP@SiO$_2$-900. b) N$_2$ adsorption/desorption isotherm of Fe/Co-N$_x$-C, with the corresponding pore size distribution shown in the inset. The results for the other materials are displayed in Figure S4 (Supporting Information).

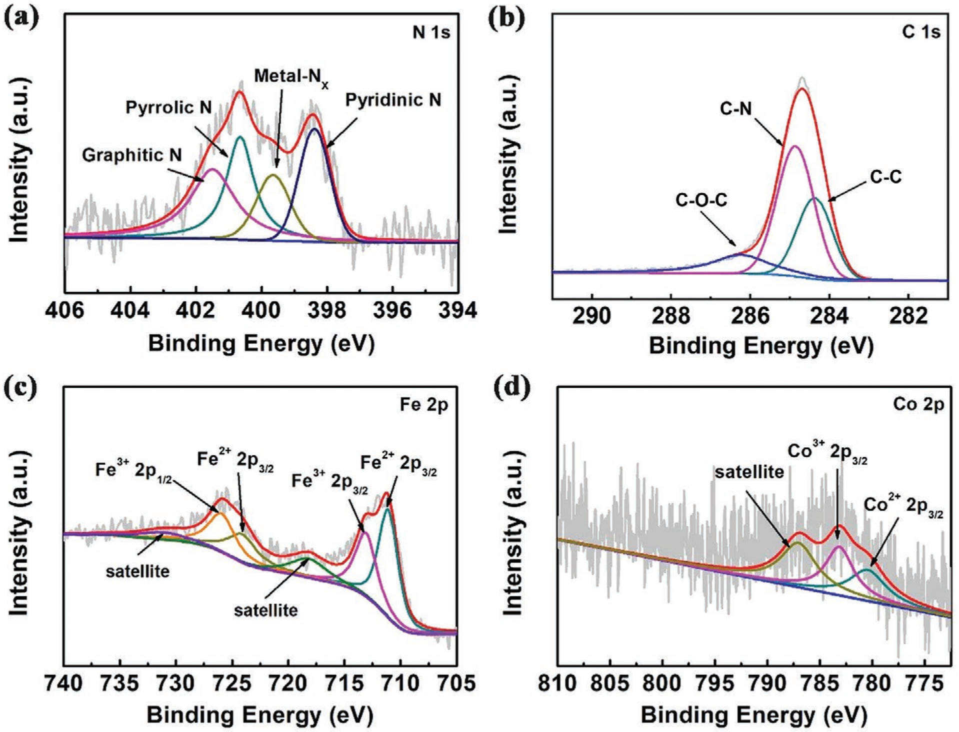

Figure 3. a–d) High-resolution XPS spectra of N 1s, C 1s, Fe 2p, and Co 2p peaks of Fe/Co-N$_x$-C.

N_2 adsorption/desorption isotherms of the materials are obtained to determine the specific surface area and porosity of Fe/Co-N$_x$-C, SiO$_2$@PP@SiO$_2$-900, SiO$_2$@FePP@SiO$_2$-900, and SiO$_2$@CoPP@SiO$_2$-900. As shown in Figure 2b and Figure S4 (Supporting Information), the isotherms are type-IV and have some hysteresis loops.[35,36] The sharp uptakes of N_2 in a mid and high relative pressure regions, which are due to capillary condensations, indicate the presence of mesopores and macrospores in the materials.[37,38] Their pore size distributions, depicted in the insets in Figure 2b and Figure S4 (Supporting Information), also show the presence of mesoporous structures in the range of 15–30 nm.

The monodisperse pores with pore sizes in the region of 15–30 nm must be associated with the removal of the silica nanoparticles templates, whose sizes are in a similar range. Based on the Brunauer–Emmett–Teller (BET) surface area analysis (Table S1, Supporting Information), the specific surface area of Fe/Co-N$_x$-C (or SiO$_2$@(Fe,Co)PP-SiO$_2$-900, which is synthesized with both silica nanoparticles templates and silica protection) is 1332 m^2 g^{-1}. This value is significantly larger than those of SiO$_2$@(Fe,Co)PP-900 (758 m^2 g^{-1}) and (Fe,Co)PP@SiO$_2$-900 (988 m^2 g^{-1}). These results indicate the major roles played by both silica template-assisted and silica-protection synthetic strategies in leading to high surface area materials. While the silica nanoparticles templates help with the formation of monodisperse mesopores, the silica protection allow the metal-modified porphyrin frameworks to maintain their well-defined structure and lead to nanostructures during pyrolysis. The BET surface area of Fe/Co-N$_x$-C (1332 m^2 g^{-1}) is also larger than those of SiO$_2$@PP@SiO$_2$-900 (1058 m^2 g^{-1}), SiO$_2$@FePP@SiO$_2$-900 (1120 m^2 g^{-1}), and SiO$_2$@CoPP@SiO$_2$-900 (1040 m^2 g^{-1}). These results indicate that having both Fe and Co species in the precursors also helps with the formation of higher surface area materials. The large specific area and porous structure in Fe/Co-N$_x$-C are expected to help with the exposure of catalytic active sites and the transfer of reactive species during electrochemical reactions.[39,40]

XPS is used to investigate the oxidation states of Fe, Co, N, and C in Fe/Co-N$_x$-C (Figure S5, Supporting Information). The XPS survey spectrum of Fe/Co-N$_x$-C (black line in Figure S5, Supporting Information) shows peaks corresponding to C, N, O, Fe, and Co elements. The high-resolution XPS spectrum of N 1s of Fe/Co-N$_x$-C (**Figure 3**a) shows peaks at 398.4, 399.6, 400.6, and 401.5 eV indicating the presence of pyridinic-N, metal-N$_x$ (N atoms coordinating with Fe/Co atoms), pyrrolic-N, and graphitic-N species. The total amount of N in Fe/Co-N$_x$-C (2.77 at%) is higher than those in SiO$_2$@PP@SiO$_2$-900 (2.32 at%), SiO$_2$@FePP@SiO$_2$-900 (1.76 at%), and SiO$_2$@CoPP@SiO$_2$-900 (1.73 at%) (Figure S6d and Table S2, Supporting Information). This indicates the higher degree of N doping in Fe/Co-N$_x$-C. Also importantly, Fe/Co-N$_x$-C possesses the highest amounts of pyridinic-N, metal-N$_x$, and graphitic-N species (Figure S6d and Table S3, Supporting Information). It is generally accepted that pyridinic-N dopant sites at the edge of the graphitic layers are effective catalytic sites for ORR because they have an ability to reduce the energy barrier for adsorption of O_2 on adjacent carbon atoms, accelerating the rate-limiting, first-electron transfer process during the ORR.[41,42] Meanwhile, the coordination of transitional metals with N-dopants in the form M-N$_x$ species generates effective electrocatalytically active sites for ORR.[43] Additionally, the presence of graphitic-N groups can improve the limiting current density of the electrocatalyst during ORR.[44,45] Previous experimental results and theoretical calculations indicated that graphitic-N dopants in carbon materials could induce nonuniform electron distributions and short C—N bonds, comparable to O—O bonds; as a result, the adsorption of O_2 and facile dis-association/weakening of O=O bonds over the material (catalyst) take place more favorably.[46,47]

Meanwhile, the high-resolution XPS spectrum of C 1s is deconvoluted into three peaks at binding energies of 284.5, 285.0, and 286.2 eV corresponding to C—C, C—N, and C—O—C functional groups, respectively (Figure 3b). The peak at ≈285.0 eV in the C 1s spectrum, which is assigned to the carbon atoms bonded with N atoms, further confirms the presence of N-dopants in the carbon material. The high-resolution Fe 2p spectrum of Fe/Co-N_x-C (Figure 3c) shows four deconvoluted peaks at 711.5, 713.4, 723.1, and 726.7 eV, which are attributable to Fe^{2+} 2p3/2, Fe^{3+} 2p3/2, Fe^{2+} 2p1/2, and Fe^{3+} 2p1/2 electrons, respectively. Two corresponding satellite peaks at 718.3 and 731.6 eV are also observed in the spectrum. These results indicate that Fe exists both as Fe^{2+} and as Fe^{3+} oxidation states in the Fe-N_x species.[48] The high-resolution Co 2p spectrum (Figure 3d) is deconvoluted into two peaks at 780.4 and 783.1 eV, corresponding to Co^{2+} 2p3/2 and Co^{3+} 2p3/2, respectively, and a satellite peak at 787.0 eV. In the spectra, no metallic Fe(0) and Co(0) species detected, which is consistent with the XRD pattern and aberration-corrected HAADF-STEM results discussed earlier. These results further demonstrate that the Fe and Co atoms are present only in the form of single atoms coordinated to the N-doped carbon matrix (or as Fe/Co-N_x species).[17]

Figure 4a and Figure S7a (Supporting Information) display the LSV curves of ORR over the materials recorded in O_2-saturated KOH solution (0.1 м) with a scan rate of 10 mV s^{-1} and a disk electrode rotating at 1600 rpm. The results show that SiO_2@PP@SiO_2-900 has a poor electrocatalytic activity for ORR with a large overpotential (Figure S7a, Supporting Information). This must be due to the relatively small pore volume, and thus low density of exposed surface catalytic active sites, and also the absence of metallic sites in it (Tables S1 and S3, Supporting Information). Compared with SiO_2@PP@SiO_2-900, SiO_2@FePP@SiO_2-900 displays a better activity for ORR, with a more positive onset potential and a larger limited current density. This must be because of the presence of catalytically active Fe-N_x sites

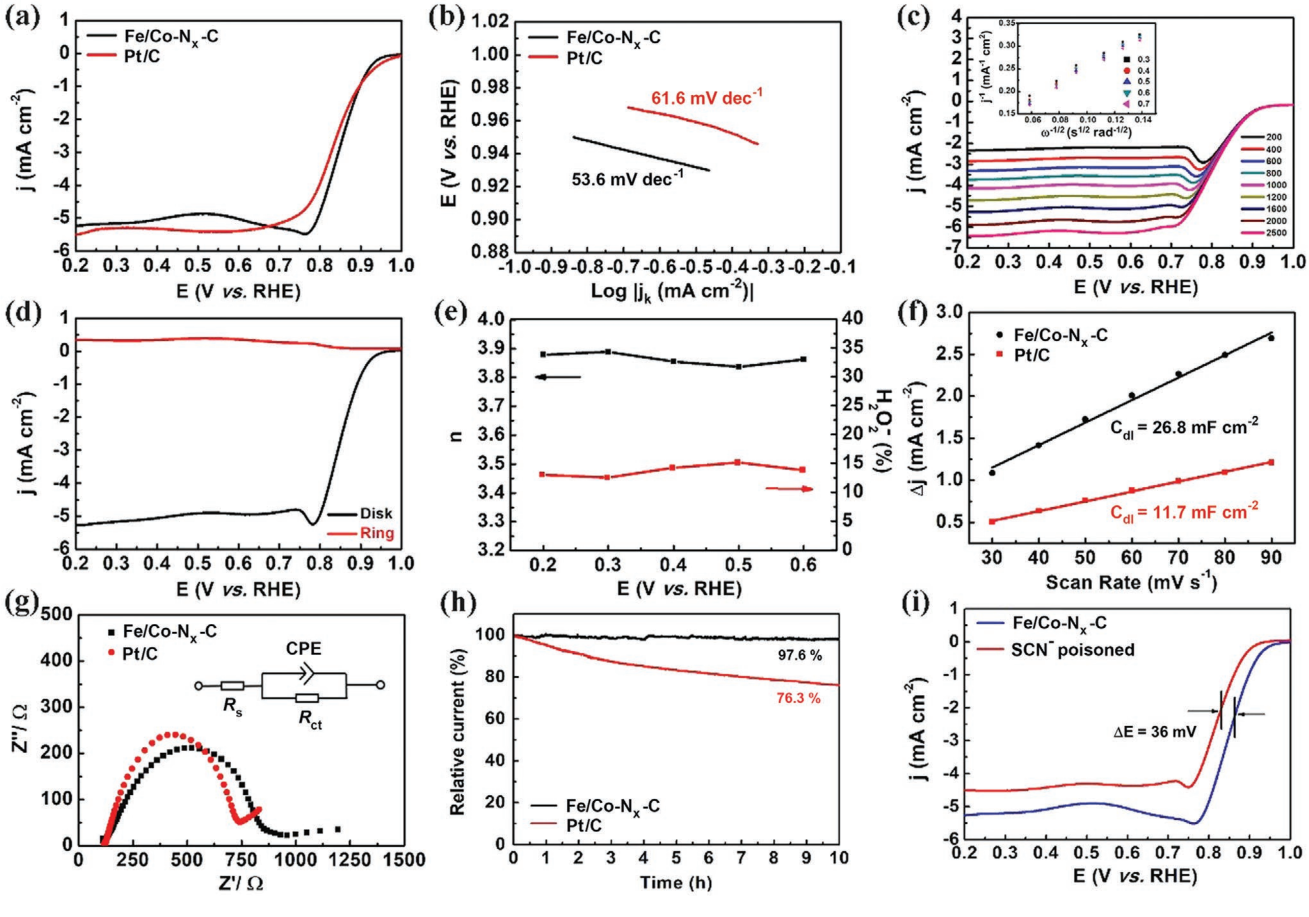

Figure 4. a) Linear sweep voltammetry (LSV) curves of ORR over Fe/Co-N_x-C and Pt/C in O_2-saturated KOH solution (0.1 м). b) The Tafel plots obtained from the LSV curves in (a). c) LSV curves of ORR over Fe/Co-N_x-C at different rotation speeds and the corresponding K–L plots (inset). d) Current density versus potential measured for ORR over Fe/Co-N_x-C with disk and ring electrodes. e) The amount of HO_2^- produced by the reaction and the electron transfer number (*n*) involved in it as measured with a RRDE. f) The values of C_{dl} for Fe/Co-N_x-C and Pt/C. g) Nyquist plots for Fe/Co-N_x-C and Pt/C, with the inset showing the corresponding equivalent circuit (where R_s, R_{ct}, and CPE represent the solution resistance, charge-transfer resistance, and constant phase element, respectively). h) Normalized chronoamperometry curves for Fe/Co-N_x-C and Pt/C. i) LSV curves of Fe/Co-N_x-C and Pt/C in O_2-saturated KOH solution (0.1 м) before and after addition of KSCN into the solution, respectively.

in it[16] as well as its higher surface area and pore volume.[39,40] However, SiO_2@CoPP@SiO_2-900 does not do the same despite its larger total pore volume. In fact its electrocatalytic activity for ORR is worse, with a larger overpotential, than that of SiO_2@PP@SiO_2-900. This can be mainly due to its lower amounts of N species, especially compared with that of SiO_2@PP@SiO_2-900 (Tables S2 and S3, Supporting Information). More interestingly, the corresponding material that has both Fe and Co (i.e., Fe/Co-N_x-C) not only possesses a larger BET specific surface area and pore volume but also has the highest amounts of total N and catalytically active N species (i.e., pyridinic-N,[41,42] graphitic-N,[44–47] and single-atom Fe/Co-N_x sites[27,43]) (Tables S1–S3, Supporting Information). This must be why it has the best activity for ORR with the most positive onset potential, the most positive half-wave potential, and the largest limiting current density (Figures S7a and Table S4, Supporting Information). The two control materials, also synthesized at 900 °C but without using silica nanoparticles templates and without silica protection (i.e., (Fe,Co)PP@SiO_2-900) and (SiO_2@(Fe,Co)PP-900, respectively), have inferior electrocatalytic activity because of their smaller BET surface areas and lower amount of active N species (see Tables S1, S3, and S4, Supporting Information). These results show the crucial roles that silica template-assisted and silica-protection synthetic strategies play in generating materials with enhanced electrocatalytic activity for ORR.

Meanwhile, the material synthesized at lower pyrolysis temperature (800 °C), SiO_2@(Fe,Co)PP@SiO_2-800, which has the largest BET surface area, displays good electrocatalytic activity for ORR (Tables S1 and S4, Supporting Information). However, its activity for ORR is still inferior to that of Fe/Co-N_x-C (or SiO_2@(Fe,Co)PP@SiO_2-900). This result reflects that the BET surface area alone is not a decisive factor in dictating the catalytic properties of the materials for ORR. It must rather be because SiO_2@(Fe,Co)PP@SiO_2-800 has much less amount of catalytic active N-based species (pyridinic-N, graphitic-N, and single-atom Fe/Co-N_x) than Fe/Co-N_x-C. The material synthesized at the highest pyrolysis temperature (1000°C), SiO_2@(Fe,Co)PP@SiO_2-1000, shows a poor electrocatalytic activity for ORR, with less positive onset and half-wave potentials, and much smaller limiting current density than both SiO_2@(Fe,Co)PP@SiO_2-800 and Fe/Co-N_x-C. This must be due to its relatively smaller surface area and lower amounts of N species (Tables S1, S3, and S4, Supporting Information).

Based on the above results, Fe/Co-N_x-C shows the best electrocatalytic activity for ORR, with the most positive onset potential (E_{onset}, 0.98 vs RHE) and half-wave potential ($E_{1/2}$, 0.860 vs RHE) (Table S4, Supporting Information) among all materials. This implies that the dual metallic species, pyrolysis temperature, silica nanoparticles templates, and silica-protection synthesis must have all directly or indirectly contributed to its high electrocatalytic activity. Although the E_{onset} of Fe/Co-N_x-C (0.98 vs RHE) is slightly less positive than that of Pt/C (1.00 V vs RHE), the former shows a more positive $E_{1/2}$ (0.860 vs RHE) than Pt/C (0.84 V vs RHE) (Figure 4a and Table S4, Supporting Information). The electrocatalytic performance, in terms of E_{onset} and $E_{1/2}$, of the as-obtained Fe/Co-N_x-C for ORR in alkaline electrolyte is also comparable to, or better than, those of many state-of-the-art ORR electrocatalysts previously reported in literature (Table S5, Supporting Information). The high electrocatalytic activity exhibited by Fe/Co-N_x-C for ORR is further verified by its smaller Tafel slope (53.6 mV dec^{-1}) compared with those of Pt/C (61.6 mV dec^{-1}) and the other control materials (see Figure 4b and Figure S7b, Supporting Information).

The kinetics of ORR on Fe/Co-N_x-C is then investigated using a RDE spinning at different rates in the range of 200–2500 rpm (Figure 4c). The corresponding Koutechy–Levich (K–L) plots display a linear relationship between the reciprocal current density (j^{-1}) and the negative square root of rotating speed ($\omega^{-1/2}$) in the potential range between 0.3 and 0.7 V versus RHE (Figure 4c inset). The results indicate that the rate of ORR over Fe/Co-N_x-C is first order.[49] The average electron transfer number of the reaction (n) over Fe/Co-N_x-C, obtained from the corresponding K–L plots, is 3.81; this indicates that the ORR, for the most part, goes through a four-electron reduction process, where O_2 is directly reduced to OH^-.

The electrochemical measurements performed using a RRDE are also used to analyze the reaction pathways of ORR over Fe/Co-N_x-C (Figure 4d). As illustrated in Figure 4e, the amount of H_2O_2 produced by ORR over this material is low (<13.9%) and the value of n is ≈3.86, suggesting an efficient four-electron transfer process. This is in line with result obtained using a RDE earlier.

The electrochemically active surface areas (ECSAs) of the materials are assessed by measuring their double-layer capacitance (C_{dl}). The value of C_{dl} is found to be 26.8 mF cm^{-2} for Fe/Co-N_x-C (Figure 4f and Table S6, Supporting Information), which is higher than those of Pt/C (11.7 mF cm^{-2}), SiO_2@(Fe,Co)PP@SiO_2-800 (11.5 mF cm^{-2}), SiO_2@(Fe,Co)PP@SiO_2-1000 (3.2 mF cm^{-2}), SiO_2@FePP@SiO_2-900 (19.0 mF cm^{-2}), SiO_2@CoPP@SiO_2-900 (22.2 mF cm^{-2}), SiO_2@PP@SiO_2-900 (20.0 mF cm^{-2}), SiO_2@(Fe,Co)PP-900 (17.2 mF cm^{-2}), and (Fe,Co)PP@SiO_2-900 (13.1 mF cm^{-2}). These results indicate that Fe/Co-N_x-C has a higher ECSA than the other materials.

EIS is employed to obtain the Nyquist plots and determine the charge transfer resistance (R_{ct}) of the materials during the reactions (Figure 4g and Figure S9, Supporting Information). Using a corresponding equivalent circuit, the value of R_{ct} for Fe/Co-N_x-C is calculated to be 798 Ω. This value is close to that of Pt/C (609 Ω) and smaller than those of the other control materials (Table S6, Supporting Information). A smaller value of R_{ct} often leads to a faster charge transfer kinetics, a lower mass transport resistance, and a better conductivity.[40] Its lower value of R_c, coupled with its higher ECSA, must have contributed to Fe/Co-N_x-C's very good electrocatalytic activity toward ORR.

ADT of Fe/Co-N_x-C during the reaction shows that it has an outstanding long-term stability. As displayed in Figure S10 (Supporting Information), the value of $E_{1/2}$ of ORR over the material changes only negligibly even after 1500 continuous reaction cycles. Chronoamperometric test performed in O_2-saturated KOH solution (0.1 м) is found to further corroborate Fe/Co-N_x-C's excellent stability during ORR (Figure 4h). After running the electrocatalytic reaction for 10 h, Fe/Co-N_x-C retains 97.6% of the initial current density (cf. a commercially available Pt/C retains only 76.3% of the initial current under the same condition, see Figure 4h).

To further confirm the role of Fe-Co dual active sites in ORR, thiocyanide (SCN^-) ions are intentionally added into the electrocatalytic reaction catalyzed by Fe/Co-N_x-C. SCN^- ions have an affinity to bind to Fe and Co atoms and severely poison or compromise the catalytic activities of the metals.[37,50–52] After addition of KSCN, the electrocatalytic activity for ORR of Fe/Co-N$_x$-C is significantly compromised, as seen by its much more negative $E_{1/2}$ and the substantially lower diffusion-limiting current density (Figure 4i). These results indirectly indicate that the atomically dispersed Fe-Co dual sites are also responsible for Fe/Co-N$_x$-C's excellent catalytic activity for ORR.

Encouraged by its good electrocatalytic properties for ORR, we further examined the electrochemical performance of Fe/Co-N$_x$-C as an electrocatalyst at air cathode in aqueous ZAB. **Figure 5**a shows a schematic illustration of the structure of an aqueous ZAB containing Fe/Co-N$_x$-C at the air electrode. As shown in Figure 5b, the ZAB with Fe/Co-N$_x$-C shows a peak power density (PPD) of 152 mW cm^{-2}. This value is much higher than that of the corresponding ZAB containing a commercially available Pt/C (whose value is 87 mW cm^{-2}). As depicted in Figure 5c, the former produces a high open-circuit voltage (OCV) of 1.42 V, and two of such ZABs connected in series can light up a 3.0 V light-emitting diode (LED), indicating the potential of this electrocatalyst for practical applications. The performance of the ZAB with Fe/Co-N$_x$-C is also compared with those of notable ZABs containing single-atom electrocatalysts recently reported in literature (Table S7, Supporting Information). The comparative results show that the performances, in terms of PPD and OCV, of our ZAB assembled with Fe/Co-N$_x$-C is comparable or even superior to those state-of-the-art single-atom catalysts-based ZABs. Furthermore, the ZAB shows only a small loss in performance when galvanostatically discharged at different current densities for long periods of time; for example, the ZAB gives off a stable voltage output of 1.27 V at the discharge current density of 2 mA cm^{-2} for over 77 h (see Figure 5d).

The rate performance of the battery is assessed by discharging it at various current densities in the range from 2 to 50 mA cm^{-2} (Figure 5e). The ZAB possessing Fe/Co-N$_x$-C as an air cathode displays minimal voltage losses of only 0.78% and 0.73% at

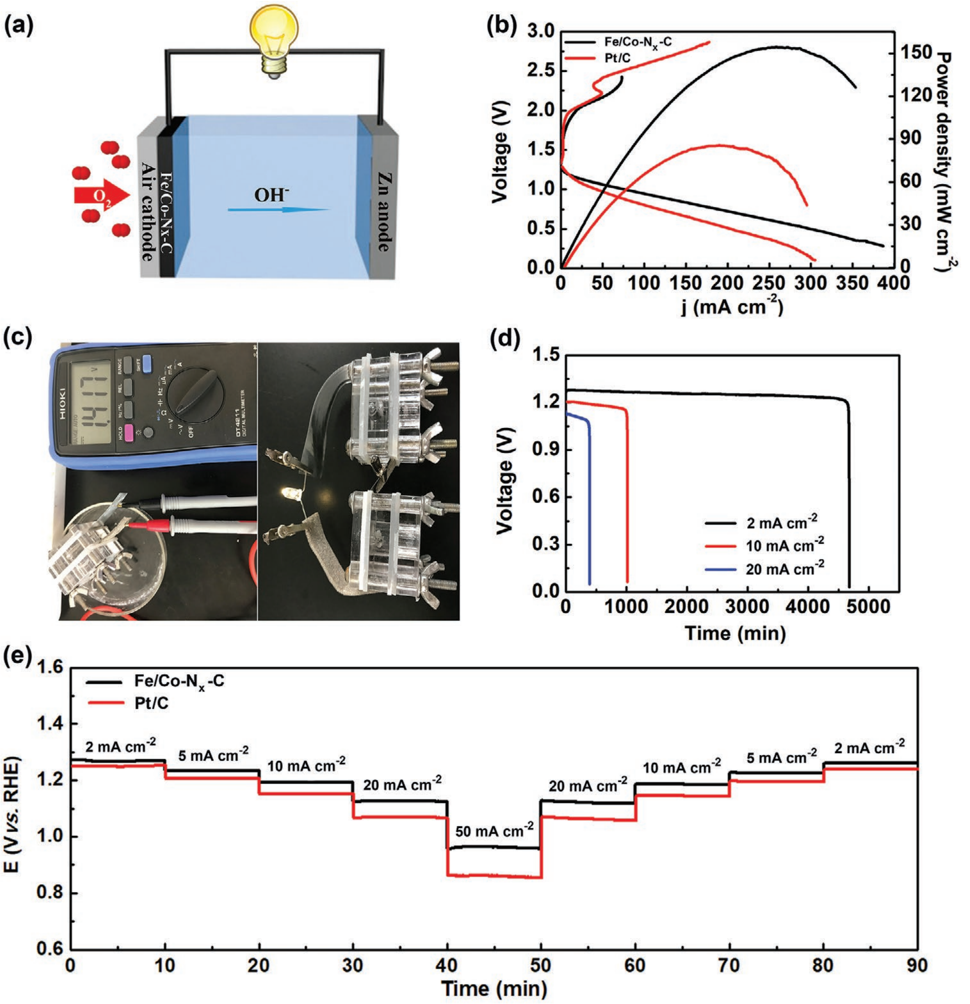

Figure 5. a) Schematic illustration of a typical aqueous ZAB containing Fe/Co-N$_x$-C as air electrode. b) LSV and power density curves of the ZABs containing Fe/Co-N$_x$-C or Pt/C as the air cathode catalyst. c) Photographs of a ZAB displaying its measured open-circuit voltage of 1.42 V and an LED powered by two such ZABs connected in series. d) Long-time galvanostatic discharge curves of ZABs with Fe/Co-N$_x$-C as the cathode catalysts at 2, 10, and 20 mA cm^{-2}. e) Discharge curves of the ZABs under different current densities (2, 5, 10, 20, and 50 mA cm^{-2}).

2.0 and 5.0 mA cm^{-2}, respectively. On the other hand, the corresponding voltage losses of the ZAB containing Pt/C are 0.49% and 0.89%, respectively. This also means, for Pt/C, the larger the discharge current density is, the greater the voltage loss is; however, for Fe/Co-N$_x$-C, the larger the discharge current density is, the smaller the voltage loss is. Furthermore, Fe/Co-N$_x$-C demonstrates an excellent stability and a good recovery property as a cathode material in a ZAB. These results confirm Fe/Co-N$_x$-C's outstanding electrocatalytic performances for ORR in ZABs, in terms of onset potential, half-wave potential, limiting current density, open-circuit potential, and durability.

All of the above results demonstrate that the dual-metal Fe/Co-N$_x$-C single-atom catalyst reported here possesses a better electrocatalytic performance for ORR in an alkaline electrolyte than the other as-generated control materials and the benchmark Pt/C catalyst under the same condition. The superior electrocatalytic performance of Fe/Co-N$_x$-C is likely to be due to the following factors: 1) its large specific surface area and high pore volume (see Table S1, Supporting Information) are conducive for the exposure of catalytic sites and mass transport of reaction-involved species;[39,40] 2) its high density of exposed N functional groups, such as pyridinic-N and graphitic-N species, along with its dual metals, create a high density of highly catalytic active Fe/Co-N$_x$ single-atom sites (Figure 1e and Figure S6d, Supporting Information);[1] 3) its large ECSA and small charge transfer resistance (Table S6, Supporting Information) provide more active sites and boost charge transfer kinetics, respectively;[40] and 4) compared with single metallic sites coordinated to N dopant atoms in carbon materials, single-atoms of bimetallic (Fe and Co) atoms coordinated to the N-dopant atoms in Fe/Co-N$_x$-C (Table S2, Supporting Information) create more favorable catalytic sites and synergistic catalytic activiities to break the bond in O$_2$ during ORR.[25–30]

4. Conclusions

In conclusion, a novel single-atom catalyst with isolated dual metal (Fe and Co) sites anchored onto hierarchically porous N-doped carbon nanonet, named Fe/Co-N$_x$-C, has been synthesized from dual metal-coordinated polyporyphyrin using a synthetic approach combining silica nanoparticles templates and silica protection. Thanks to its large specific surface area, high amount of active N species (pridinic-N, metal-N$_x$, and graphitic-N groups), homogeneously dispersed Fe/Co-N$_x$ bimetallic single-atom sites, large electrochemical surface area, and high electronical conductivity, Fe/Co-N$_x$-C catalyst displayed outstanding electrocatalytic performance for ORR in alkaline media with more positive half-wave potential and much better long-term stability than the commercially available Pt/C catalyst. Furthermore, the material was demonstrated to serve as an efficient, nonprecious, and stable metal catalyst as the air cathode in ZAB, producing excellent power density while remaining stabile for hours. This demonstrates the potential practical application of the as-prepared Fe/Co-N$_x$-C catalyst in renewable energy devices. The work has also demonstrated a new approach for rational design and synthesis of highly efficient noble metal-free electrocatalysts for energy storage and conversion applications.

Supporting Information

Supporting Information is available from the Wiley Online Library or from the author.

Acknowledgements

This work was supported by International Cooperation Project of Jilin Province (20190701022GH) and National Natural Science Foundation of China (51872115).

Conflict of Interest

The authors declare no conflict of interest.

Keywords

Fe/Co-coordinated polyporphyrin, oxygen reduction reaction, silica templates, single-atom catalysts, zinc–air batteries

Received: February 5, 2020
Revised: June 28, 2020

---

[1] M. Liu, L. Wang, K. Zhao, S. Shi, Q. Shao, L. Zhang, X. Sun, Y. Zhao, J. Zhang, *Energy Environ. Sci.* **2019**, *12*, 2890.
[2] D. Yang, L. Zhang, X. Yan, X. Yao, *Small* **2017**, *1*, 1700209.
[3] M. Shao, Q. Chang, J. P. Dodelet, R. Chenitz, *Chem. Rev.* **2016**, *116*, 3594.
[4] W. Li, C. Min, F. Tan, Z. Li, B. Zhang, R. Si, M. Xu, W. Liu, L. Zhou, Q. Wei, *ACS Nano* **2019**, *13*, 3177.
[5] X. Fu, N. Li, B. Ren, G. Jiang, Y. Liu, F. M. Hassan, D. Su, J. Zhu, L. Yang, Z. Bai, *Adv. Energy Mater.* **2019**, *9*, 1803737.
[6] S. Yasuda, A. Furuya, Y. Uchibori, J. Kim, K. Murakoshi, *Adv. Funct. Mater.* **2016**, *26*, 738.
[7] A. Zitolo, V. Goellner, V. Armel, M. T. Sougrati, T. Mineva, L. Stievano, E. Fonda, F. Jaouen, *Nat. Mater.* **2015**, *14*, 937.
[8] J. Masa, W. Xia, M. Muhler, W. Schuhmann, *Angew. Chem., Int. Ed.* **2015**, *54*, 10102.
[9] Z. Huang, H. Pan, W. Yang, H. Zhou, N. Gao, C. Fu, S. Li, H. Li, Y. Kuang, *ACS Nano* **2018**, *12*, 208.
[10] S. Fu, C. Zhu, D. Su, J. Song, S. Yao, S. Feng, M. H. Engelhard, D. Du, Y. Lin, *Small* **2018**, *14*, 1703118.
[11] C. Zhu, Q. Shi, B. Z. Xu, S. Fu, G. Wan, C. Yang, S. Yao, J. Song, H. Zhou, D. Du, *Adv. Energy Mater.* **2018**, *8*, 1801956.
[12] M. Chen, Y. He, J. S. Spendelow, G. Wu, *ACS Energy Lett.* **2019**, *4*, 1619.
[13] C. Zhu, S. Fu, Q. Shi, D. Du, Y. Lin, *Angew. Chem., Int. Ed.* **2017**, *56*, 13944.
[14] B.-Q. Li, C.-X. Zhao, S. Chen, J.-N. Liu, X. Chen, L. Song, Q. Zhang, *Adv. Mater.* **2019**, *31*, 1900592.
[15] B.-Q. Li, S.-Y. Zhang, B. Wang, Z.-J. Xia, C. Tang, Q. Zhang, *Energy Environ. Sci.* **2018**, *11*, 1723.
[16] H. Xu, D. Cheng, D. Cao, X. C. Zeng, *Nat. Catal.* **2018**, *1*, 339.
[17] Y. Chen, S. Ji, Y. Wang, J. Dong, W. Chen, Z. Li, R. Shen, L. Zheng, Z. Zhuang, D. Wang, Y. Li, *Angew. Chem., Int. Ed.* **2017**, *56*, 6937.
[18] D. Liu, J. C. Li, Q. Shi, S. Feng, Z. Lyu, S. Ding, L. Hao, Q. Zhang, C. Wang, M. Xu, T. Li, E. Sarnello, D. Du, Y. Lin, *ACS Appl. Mater. Interfaces* **2019**, *11*, 39820.

[19] J. Han, X. Meng, L. Lu, J. Bian, Z. Li, C. Sun, *Adv. Funct. Mater.* **2019**, *29*, 1808872.

[20] Y. Pan, S. Liu, K. Sun, X. Chen, B. Wang, K. Wu, X. Cao, W. C. Cheong, R. Shen, A. Han, Z. Chen, L. Zheng, J. Luo, Y. Lin, Y. Liu, D. Wang, Q. Peng, Q. Zhang, C. Chen, Y. Li, *Angew. Chem., Int. Ed.* **2018**, *57*, 8614.

[21] P. Yin, T. Yao, Y. Wu, L. Zheng, Y. Lin, W. Liu, H. Ju, J. Zhu, X. Hong, Z. Deng, G. Zhou, S. Wei, Y. Li, *Angew. Chem., Int. Ed.* **2016**, *55*, 1.

[22] G. Han, Y. Zheng, X. Zhang, Z. Wang, Y. Gong, C. Du, M. N. Banise, Y. M. Yiu, T. K. Sham, L. Gu, Y. Sun, Y. Wang, J. Wang, Y. Gao, G. Yin, X. Sun, *Nano Energy* **2019**, *66*, 104088.

[23] Y. Qu, Z. Li, W. Chen, Y. Lin, T. Yuan, Z. Yang, C. Zhao, J. Wang, C. Zhao, X. Wang, F. Zhou, Z. Zhuang, Y. Wu, Y. Li, *Nat. Catal.* **2018**, *1*, 781.

[24] L. Yang, L. Shi, D. Wang, Y. Lv, D. Cao, *Nano Energy* **2018**, *50*, 691.

[25] M. Xiao, H. Zhang, Y. Chen, J. Zhu, L. Gao, Z. Jin, J. Ge, Z. Jiang, S. Chen, C. Liu, W. Xing, *Nano Energy* **2018**, *46*, 396.

[26] E. F. Holby, C. D. Taylor, *Sci. Rep.* **2015**, *5*, 9286.

[27] J. Wang, Z. Huang, W. Liu, C. Chang, H. Tang, Z. Li, W. Chen, C. Jia, T. Yao, S. Wei, Y. Wu, Y. Li, *J. Am. Chem. Soc.* **2017**, *139*, 17281.

[28] Z. Lu, B. Wang, Y. Hu, W. Liu, Y. Zhao, R. Yang, Z. Li, J. Luo, B. Chi, Z. Jiang, M. Li, S. Mu, S. Liao, J. Zhang, X. Sun, *Angew. Chem., Int. Ed.* **2019**, *58*, 2622.

[29] D. Zhang, W. Chen, Z. Li, Y. Chen, L. Zheng, Y. Gong, Q. Li, R. Shen, Y. Han, W. C. Cheong, L. Gu, Y. Li, *Chem. Commun.* **2018**, *54*, 4274.

[30] S. Gong, C. Wang, P. Jiang, L. Hu, H. Lei, Q. Chen, *J. Mater. Chem. A* **2018**, *6*, 13254.

[31] Y. Yang, H. Zhang, Z. Liang, Y. Yin, B. Mei, F. Song, F. Sun, S. Gu, Z. Jiang, Y. Wu, Z. Zhu, *J. Energy Chem.* **2020**, *44*, 131.

[32] H. W. Liang, W. Wei, Z. S. Wu, X. Feng, K. Müllen, *J. Mater. Chem. A* **2013**, *135*, 16002.

[33] Y. Hou, Z. Wen, S. Cui, S. Ci, S. Mao, J. Chen, *Adv. Funct. Mater.* **2015**, *25*, 872.

[34] J. Zhu, H. Zhou, C. Zhang, J. Zhang, S. Mu, *Nanoscale* **2017**, *9*, 13257.

[35] H. Li, X. Qian, C. Zhu, X. Jiang, L. Shao, L. Hou, *J. Mater. Chem. A* **2017**, *5*, 4513.

[36] Q. Lai, J. Zhu, Y. Zhao, Y. Liang, J. He, J. Chen, *Small* **2017**, *13*, 1700740.

[37] J. Ding, P. Wang, S. Ji, H. Wang, V. Linkov, R. Wang, *Electrochim. Acta* **2019**, *296*, 653.

[38] N. Ramaswamy, U. Tylus, Q. Jia, S. Mukerjee, *J. Am. Chem. Soc.* **2013**, *135*, 15443.

[39] W. Zhou, J. Jia, J. Lu, L. Yang, D. Hou, G. Li, *Nano Energy* **2016**, *28*, 29.

[40] S. Zheng, F. Fang, G. Zhou, G. Chen, L. Ouyang, M. Zhu, D. Sun, *Chem. Mater.* **2008**, *20*, 3954.

[41] H. W. Liang, X. D. Zhuang, S. Brüller, X. L. Feng, K. Müllen, *Nat. Commun.* **2014**, *5*, 4973.

[42] T. Ikeda, M. Boero, S. F. Huang, K. Terakura, M. Oshima, J. Ozak, *J. Phys. Chem. C* **2008**, *112*, 14706.

[43] D. Deng, L. Yu, X. Chen, G. Wang, L. Jin, X. Pan, J. Deng, G. Sun, X. Bao, *J. Mater. Chem. A* **2013**, *1*, 14868.

[44] J. W. Zhu, H. Zhou, C. T. Zhang, J. Zhang, S. C. Mu, *Nanoscale* **2017**, *9*, 13257.

[45] L. Lai, J. R. Potts, D. Zhan, L. Wang, C. K. Poh, C. Tang, H. Gong, Z. Shen, J. Linc, R. S. Ruoff, *Energy Environ. Sci.* **2012**, *5*, 7936.

[46] R. A. Sidik, A. B. Anderson, N. P. Subramanian, S. P. Kumaraguru, B. N. Popov, *J. Phys. Chem. B* **2006**, *110*, 1787.

[47] R. Liu, D. Wu, X. Feng, K. Müllen, *Angew. Chem., Int. Ed.* **2010**, *49*, 2565.

[48] Z. S. Wu, S. Yang, Y. Sun, K. Parvez, X. Feng, K. Müllen, *J. Am. Chem. Soc.* **2012**, *134*, 9082.

[49] Y. Qian, T. An, K. E. Birgersson, Z. Liu, D. Zhao, *Small* **2018**, *14*, 1704169.

[50] L. T. Song, Z. Y. Wu, F. Zhou, H. W. Liang, Z. Y. Yu, S. H. Yu, *Small* **2016**, *12*, 6398.

[51] T. Sun, S. Zhao, W. Chen, D. Zhai, J. Dong, Y. Wang, Y. Li, *Proc. Natl. Acad. Sci. USA* **2018**, *115*, 12692.

[52] X. Wan, H. Wang, H. Yu, F. Peng, *J. Power Sources* **2017**, *346*, 80.